NEOPLASMA accepted, ahead of print manuscript
Cite article as https://doi.org/10.4149/neo_2026_260713N236

Running title: Spatial TIME heterogeneity in gastric cancer

Spatial heterogeneity of the tumor immune microenvironment in gastric cancer: exploratory associations with clinicopathological features

Lina Shang[1,2,#], Jiaming Dong[1,#], Wei Liu[1,3], Yun Dang[1,4], Cunpu Du[1], Chanyuan Zhao[1], Quan Zhou[1], Chenli Zhang[1,3], Xiaoyu Zhang[1,5], Chenyu Wang[1,3], Aijun Yang[1,3,*], Min Wang[1,3,6,*], Min Li [1,3,7,*]

[1]Institute of Pathology, School of Basic Medical Sciences, Lanzhou University, Lanzhou, China; [2]Medical College of Northwest Minzu University, Lanzhou, China; [3]The Forensic Identification Unit of Lanzhou University, Lanzhou, China; [4]Gansu Provincial Maternity and Child-care Hospital/Gansu Provincial Central Hospital, Lanzhou, China; [5]Institute of Anatomy and Histology and Embryology, Neuroscience, School of Basic Medical Sciences, Lanzhou University, Lanzhou, China; [6]Experimental Teaching Center of Basic Medicine, School of Basic Medical Sciences, Lanzhou University, Lanzhou, China; [7]Key Laboratory of Preclinical Study for New Drugs of Gansu Province, Lanzhou University, Lanzhou, China

*Correspondence: limin@lzu.edu.cn; wmin@lzu.edu.cn; yangaijun999@126.com

[#]Contributed equally to this work.

Received July 13, 2026 / Accepted October 21, 2026

We aimed to describe the spatial heterogeneity of selected immune-cell populations and stromal markers within the tumor immune microenvironment (TIME) of gastric cancer and to explore their associations with clinicopathological features.

CD8, CD20, CD163, FOXP3, PD-1, and SMA were assessed by immunohistochemistry in 102 resected gastric cancer specimens. Positive cells were quantified, and SMA was semi-quantitatively scored, in the tumor center (TC), inner invasive margin (IIM), and outer invasive margin (OIM). Exploratory clustering of CD8/CD20-enriched and CD163/FOXP3-enriched cell proportions was used to define exploratory TIME pattern groups (CD8/CD20-enriched, CD163/FOXP3-enriched, and intermediate); heterogeneity grades were based on group consistency across regions. Associations with clinicopathological features and survival were analyzed.

CD163+ macrophage-like cells predominated, but their proportion decreased from TC to OIM ($p < 0.001$), whereas the proportion of CD20+ B cells increased ($p < 0.001$). Moderate/high heterogeneity was observed in 69% of cases. In the OIM, the distribution of exploratory TIME pattern groups was associated with lymph node metastasis, deeper invasion, and advanced TNM stage (all $p < 0.001$), but survival differences were not statistically significant. PD-1+ cell density peaked in the OIM ($p < 0.001$), and the PD-1/CD8 ratio was higher in both TC and OIM than in IIM. In the OIM, the CD8/CD20-enriched pattern had the highest PD-1+ cell density and the CD163/FOXP3-enriched pattern the lowest ($p < 0.05$), with no significant differences in TC and

manuscript

IIM. SMA+ stromal scores decreased from TC to OIM, were highest in the CD163/FOXP3-enriched pattern, and were inversely associated with CD8+ T cell and CD20+ B cell densities.
In conclusion, gastric cancer exhibits a structured, non-random spatial immune microenvironment, with the TC and invasive margins representing immunologically distinct compartments. PD-1 expression and stromal components show region-specific features within this spatial immune landscape. These findings reveal exploratory associations with clinicopathological features and provide a basis for further validation in independent cohorts.

Key words: gastric cancer; tumor immune microenvironment; spatial heterogenity; immune cells; cancer-associated fibroblasts

The heterogeneity of the tumor immune microenvironment (TIME) refers to the differences in gene expression, infiltration abundance, and immune factor expression levels of immune cells within the TIME [1-3], exhibiting both spatial and temporal heterogeneity. Spatial heterogeneity in the TIME refers to variations in the localization or abundance/activity of TIME components across different spatial regions. Evidence suggests that sensitivity to immunotherapy may vary significantly depending on the heterogeneity of neoantigens, antigen presentation mechanisms, or cytotoxic signaling pathways within the TIME [4, 5]. Therefore, TIME heterogeneity can influence the efficacy of immunotherapy in patients with solid tumors. TIME heterogeneity is crucial to improving the effectiveness of tumor immunotherapy. Gastric cancer is a malignant tumor originating from the epithelial cells of the gastric mucosa and glands. Current treatment options for advanced-stage disease include chemoradiotherapy, targeted therapy, and immunotherapy for advanced stages. However, the overall survival rate remains low [6, 7]. Suboptimal post-treatment survival has been associated with the heterogeneity of the tumor and its immune microenvironment [8].

Immune cells, such as tumor-associated macrophages (TAMs), T lymphocytes, and B cells, are crucial components of the TIME. The cell types and infiltration levels significantly influence the efficacy of immunotherapy [9]. M_2-type TAMs and regulatory T cells (Tregs) have been associated with immunosuppressive functions, while $CD8^+$ T cells and B cells have been associated with anti-tumor roles. There is significant spatial heterogeneity in the distribution of M2-type TAMs [10, 11], $CD8^+$ T cells [12, 13], Tregs [14], and B cells [14] within the TIME, and the effects of these cells on tumors vary depending on their spatial locations. Existing research largely addresses spatial heterogeneity of individual immune cell types, while the spatial heterogeneity of the multi-cellular

Accepted manuscript

TIME and its effects on tumors remain unclear. Therefore, under the framework of gastric cancer histomorphology, this study describes the spatial heterogeneity of selected immune-cell populations and stromal markers, explores TIME pattern groups, and examines their associations with clinicopathological features, aiming to offer new insights into the spatial heterogeneity of the TIME in gastric cancer.

Patients and methods

Sample collection. A total of 163 paraffin-embedded tissue blocks from gastric cancer patients who underwent surgery between December 2019 and December 2020 were collected. All patients were preoperatively diagnosed with gastric adenocarcinoma without neoadjuvant therapy. Following immunohistochemical staining, 102 cases were included in the clinicopathological analysis, and 50 cases with complete survival data were included in the survival analysis (Supplementary Figure S1 for the detailed selection and exclusion process). Baseline characteristics are summarized in Supplementary Table S1. Potential selection bias was assessed by comparing clinicopathological features between included and excluded cases.

Overall survival (OS) was defined as the time from surgery to death from any cause, with censoring on December 8, 2024. This study was approved by the Medical Ethics Committee of the School of Basic Medical Sciences, Lanzhou University (Approval No. Lzujcyxy20240341), and the requirement for written informed consent was waived due to the retrospective design using anonymized data.

Reagents. The primary antibodies used for immunohistochemistry were anti-CD8, anti-CD20, anti-CD163, anti-FOXP3, anti-Ki-67, anti-SMA, and anti-PD-1. Detailed antibody information is provided in Supplementary Table S2.

Immunohistochemistry. 3-4 μm paraffin sections were dewaxed, rehydrated, subjected to antigen retrieval in EDTA buffer under high pressure for 3 min, blocked to quench endogenous peroxidase activity, incubated with primary antibodies overnight at 4 °C, detected using an amplification reagent and DAB chromogen, and counterstained with hematoxylin.

Digitalization and tissue region definition. Stained sections were scanned using a digital slide scanning system (3DHISTECH, Hungary). After tissue-loss cases were excluded, 102 cases were analyzed for CD8, CD20, CD163, and FOXP3 expression. Three tumor-related regions were

Accepted manuscript

defined according to previous reports [15-18]. The inner two-thirds of the distance from the tumor center to the margin constituted the tumor center (TC), while the outer one-third was the inner invasive margin (IIM), and the area of adjacent stroma within 1 mm outside the margin was the outer invasive margin (OIM) (Supplementary Figure S2). For each region, five fields were randomly selected at 40× magnification using Case Viewer software. The investigators who selected the fields and performed the digital image analysis were blinded to the patients' clinical outcomes.

Quantification of immune cells, Ki-67, and PD-1. All digital analyses used the Quant Center function of Case Viewer software. For CD8, CD20, CD163, FOXP3, and PD-1, the "Histo" module identified positive cells (brown) and calculated positive cells/mm² after cell size filtration [19]. PD-1-positive cells were similarly quantified within stromal regions. For Ki-67, the "Nuclei" module was applied to distinguish positive (brown) and negative (blue) tumor cell nuclei, with stromal nuclei excluded by size gating.

Association of Ki-67 status, tumor differentiation, and depth of invasion with immune cell infiltration. A total of 102 gastric cancer cases were included in this study. Based on previous literature [20-22], a Ki-67 index > 45% was defined as High, and ≤ 45% as Low. Given the heterogeneous expression of Ki-67 within the same tumor region, five random fields of view (FOVs) were selected per region. Patients in whom all five FOVs were uniformly classified as either High or Low were excluded to ensure the presence of both proliferative states within the sampled regions. For each included patient, the average immune cell density was calculated separately for the Ki-67 High FOVs and the Ki-67 Low FOVs for subsequent statistical analysis.

Similarly, to evaluate the spatial association between tumor differentiation and immune cell infiltration, the histological differentiation status (moderately differentiated vs. poorly differentiated) was independently assessed for each of the five FOVs within a region. Patients whose five FOVs did not include both differentiation states were excluded. The average immune cell density was calculated separately for the moderately differentiated FOVs and the poorly differentiated FOVs within the same region for paired comparisons.

Furthermore, to evaluate the association between the depth of invasion and immune cell infiltration, the depth of invasion was categorized into two groups: MS (mucosa and submucosa) and MA (muscularis and adventitia). For each patient, the immune cell density within the MS and MA regions was calculated as the average of five randomly selected FOVs. The average immune cell

Accepted manuscript

densities were then compared between the MS and MA groups for subsequent statistical analysis.

Exploratory TIME pattern grouping by clustering analysis. A total of 102 gastric cancer patients were included, with five random fields of view (FOVs) selected from each of the TC, IIM, and OIM regions. FOVs with insufficient tissue for evaluation were excluded. Proportions of CD8/CD20-enriched ($CD8^+$ T cells and $CD20^+$ B cells) and CD163/FOXP3-enriched ($CD163^+$ macrophage-like cells and $FOXP3^+$ T cells) cells were calculated for each FOV. Given the compositional nature of these data, the two proportions were transformed using the log-ratio (log(CD8/CD20/CD163/FOXP3)), which is equivalent to a centered log-ratio (CLR) transformation for two components to normalize the input variables.

To explore the spatial landscape of the tumor microenvironment without a priori assumptions, an exploratory unsupervised hierarchical clustering approach was performed at the FOV level using the stats::hclust function in R (version 4.5.0) with Euclidean distance and complete linkage. The clustering solution was inspected, and k=3 was selected based on the dendrogram structure and consistency with previously described frameworks [23-25] To assess the robustness of the data-driven clustering and determine whether it could define stable clinical categories, cluster stability was evaluated using bootstrap resampling with 100 iterations via the fpc::clusterboot package in R, and the mean Jaccard similarity was calculated for each cluster.

Given that exploratory clustering alone may not always yield clinically reproducible boundaries, we subsequently applied predefined threshold-based rules ($\geq$ 60%, $<$ 40%, and 40-60%) based on established frameworks [23-25] to the original CD8/CD20 proportions to define the final exploratory TIME pattern groups. Consequently, each FOV was assigned a single exploratory TIME pattern: CD8/CD20-enriched, CD163/FOXP3-enriched, or intermediate. The consistency between the exploratory clustering results and the threshold-based classification was evaluated to ensure both data-driven robustness and clinical applicability. To align with clinicopathological assessment and avoid pseudoreplication in subsequent statistical analyses, we aggregated the FOV-level classifications to the regional level, as detailed in the following sections. Heatmaps were generated using the gplots package to visualize the clustering results.

Evaluation of exploratory TIME patterns and PD-1 expression. For PD-1 analysis, the exploratory TIME pattern of each region (TC, IIM, and OIM) was evaluated in five randomly selected fields of view (FOVs). To avoid potential sampling bias and align with routine pathological

assessment protocols, a single representative TIME pattern was assigned to each region based on the majority vote of its five FOVs (a pattern present in at least 3 of 5 FOVs was defined as the region-dominant pattern). The PD-1^+ cell counts across the five FOVs were averaged to represent the regional PD-1 level. Patients with missing PD-1 data in a specific region were excluded from the corresponding regional analysis. Consequently, each patient contributed one data point per region, which represented the association between the region-specific TIME pattern and PD-1 expression.

Semi-quantitative assessment of SMA^+ stromal cells. SMA staining was assessed in the tumor stromal compartment. The muscularis mucosae, muscularis propria, and perivascular regions were not included in the areas scored. Due to irregular cell morphology, SMA staining was scored semi-quantitatively by two independent pathologists in a double-blind manner in the same fields used for immune cell quantification. A validated scoring system [26] combining staining intensity (1, weak; 2, moderate; 3, strong) and positive area pe combining staining intensity (1, weak; 2, moderate; 3, strong) and positive area percentage (0, ≤ 10%; 1, 11-25%; 2, 26-50%; 3, 51-75%; 4, > 75%) was applied. The final SMA+ stromal cell score was the product of the intensity and percentage scores, ranging from 0 to 12. Inter-observer agreement for SMA scoring was assessed in 30 cases. The simple Kappa coefficient was 0.807, the quadratic weighted Kappa was 0.987, and the intraclass correlation coefficient (ICC; two-way random effects, absolute agreement, single rater) was 0.981 (95%CI: 0.961-0.991), indicating almost perfect agreement between the two pathologists. For each patient, SMA staining was scored in the same five fields of view (FOVs) used for immune cell quantification across the TC, IIM, and OIM regions. To evaluate the association between exploratory TIME patterns and SMA scores, we determined the representative TIME pattern for each region using the same consensus strategy (majority vote, i.e., a pattern present in at least 3 of 5 FOVs) as described for PD-1. The average SMA score of the five FOVs was calculated to represent the regional SMA level. Patients with missing SMA data in a specific region were excluded from the corresponding analysis. Consequently, each patient contributed one data point per region for analysis of the association between the region-specific TIME pattern and SMA expression.

Classification of TIME heterogeneity levels. TIME heterogeneity was assessed by comparing subtypes across the three regions. Grade I was defined as consistent subtypes in all regions; Grade II as two distinct subtypes among the three regions; and Grade III as all three subtypes.

Accepted manuscript

Bioinformatics analysis. RNA sequencing expression data (FPKM-UQ) and corresponding clinical information for TCGA-STAD cases were downloaded from the UCSC Xena portal (https://xenabrowser.nCIet). Deconvolution was performed using the CIBERSORTx algorithm via the TIMER2.0 web server (https://timer.cistrome.org/) with the LM22 signature matrix and 100 permutations; only samples with deconvolution $p < 0.05$ were retained. The relative proportions of immune cell populations were extracted for downstream comparison. Because conventional TCGA data are derived from bulk tissue without matched tumor-center and invasive-margin sampling, this analysis provides indirect external support only and cannot validate spatial patterns.

Statistical analysis. Data were analyzed using GraphPad Prism 8 (GraphPad Software, San Diego, CA, USA) and R software (version 4.5.0), with graphs generated using GraphPad Prism 8 and R packages (including ggplot2, pheatmap, gplots, and forestplot). For categorical variables, comparisons were performed using the Chi-square test or Fisher's exact test (when expected count < 5), and results were reported as proportions with 95% confidence intervals (CIs) where applicable, p-values, and Cramer's V. For two-group paired comparisons, the Wilcoxon matched-pairs signed rank test was used, and results were reported as median differences with 95% CIs and p-values. For two-group unpaired comparisons, the Mann-Whitney U test was used, and results were reported as effect sizes (rank-biserial correlation coefficient, r), p-values, *U* values, and sample sizes (n). For multiple paired comparisons, the Friedman test was performed followed by post-hoc pairwise Wilcoxon matched-pairs signed rank tests with Benjamini-Hochberg (BH) FDR correction, and results were reported as raw p-values, median differences with 95%CIs, and FDR-adjusted q values. For multiple unpaired comparisons, the Kruskal-Walli's test was performed followed by Dunn's multiple comparison test, and results were reported as effect sizes (*r*) and adjusted p-values. Correlation analyses were performed using Spearman's rank correlation, and results were reported as Spearman's rho with 95%CIs (calculated via Fisher's z-transformation), raw p-values, and FDR-adjusted q values. Clustering and stability analysis were performed as described in the previous section. Survival analyses, including Kaplan-Meier curves and univariate/multivariate Cox proportional hazards regression models, were performed using R packages (survival and survminer), and results were reported as p-values and hazard ratios (HRs) with 95%CIs, with multivariate models adjusted for relevant clinicopathological factors. A two-sided p-value < 0.05 was considered statistically significant, except for correlation analyses where a BH-adjusted $q < 0.05$ was applied

Accepted manuscript

231 and for multiple paired comparisons where a BH-adjusted $q < 0.01$ was applied.

232

233

Accepted manuscript

Results

Spatial distribution and composition of immune cells. Among the 163 initially collected cases, 102 were eligible for spatial analysis after technical exclusion. Baseline comparison showed no significant differences between included and excluded cases ($p > 0.05$; Supplementary Table S3), except for perineural invasion ($p=0.02$), suggesting no substantial selection bias.

The density of $CD8^+$ T cells increased progressively with distance from the TC, peaking in the OIM ($q < 0.01/0.001$). The density of $CD163^+$ macrophage-like cells did not differ significantly among the three zones ($q > 0.01$). The densities of $CD20^+$ B cells and those of $FOXP3^+$ T cells did not differ significantly between TC and IIM, but were predominantly enriched in the OIM ($q < 0.01/0.001$; Supplementary Figure S3; Supplementary Table S4). Overall, $CD163^+$ macrophage-like cells exhibited the highest density and proportion across all three regions (adjusted $p < 0.001$; Figures 1A-1C; Supplementary Figure S4; Supplementary Tables S5 and S6). Among the remaining three cell types, $CD8^+$ T cells showed significantly higher density and proportion than $CD20^+$ B cells in the TC and IIM (adjusted $p < 0.001$), but comparable levels in the OIM (ns). Additionally, $CD8^+$ T cells consistently exceeded $FOXP3^+$ T cells across all three regions (adjusted $p < 0.001$). Notably, $CD20^+$ B cells and $FOXP3^+$ T cells had comparable density and proportion in the TC and IIM (ns), whereas $CD20^+$ B cells significantly surpassed $FOXP3^+$ T cells in the OIM (adjusted $p < 0.001$; Figures 1A-1C; Supplementary Figure S4; Supplementary Tables 5 and 6). These findings were consistent with TCGA data (Figure 1D). Notably, the proportion of $CD20^+$ B cells was significantly elevated in the OIM compared to both the TC and IIM ($q < 0.01$, Figure 1E; Supplementary Table S7), whereas the proportion of $CD163^+$ macrophage-like cells was significantly reduced in the OIM relative to the other two zones ($q < 0.001$, Figure 1E; Supplementary Table S7). In contrast, the proportions of $CD8^+$ T cells and those of $FOXP3^+$ T cells did not differ significantly among the three zones (ns, $q \geq 0.01$, Figure 1E; Supplementary Table S7). Together, these data reveal a spatial gradient in immune cell density and composition.

Functional correlates of spatial structural heterogeneity. We next examined whether this structural heterogeneity was accompanied by differences in immune cell associations. Assessment of immune cell densities (Supplementary Figure S5A-S5C; Supplementary Table S8) revealed that $CD163^+$ macrophage-like cells positively correlated with $CD8^+$ T cells across all zones (all $q < 0.01$). Similarly, $CD163^+$ macrophage-like cells positively correlated with $CD20^+$ B cells in the TC

Accepted manuscript

and IIM (both $q < 0.01$), but not in the OIM ($q > 0.01$). Furthermore, positive correlations with $FOXP3^+$ T cells were observed in the TC and OIM (both $q < 0.01$), but not in the IIM ($q > 0.01$). Collectively, these findings reveal region-dependent associations in the densities of these immune cell markers.

We further assessed the association between Ki-67 status and immune cell densities. No significant differences were found between the Ki-67 High and Low groups for $CD8^+$, $CD20^+$, $CD163^+$, or $FOXP3^+$ cells across the TC, IIM, and OIM regions (all $p > 0.05$, Figure 2; Supplementary Figures S6, S7; Supplementary Table S9). Regarding invasion depth (Supplementary Figures S8, S9; Supplementary Table S10), $CD163^+$ macrophage-like cells increased significantly with deeper layers in both IIM and OIM ($p < 0.01$); conversely, $CD20^+$ B cells decreased in the deep OIM layers ($p < 0.05$) but remained unchanged in the IIM, while $CD8^+$ T cells and $FOXP3^+$ T cells showed no variation. For differentiation status (Supplementary Figures S10-S12; Supplementary Table S11), no statistically significant differences were observed in the densities of $CD8^+$ T cells, $CD20^+$ B cells, $CD163^+$ macrophage-like cells, or $FOXP3^+$ T cells between the moderately-differentiated and poorly-differentiated groups across the TC, IIM, and OIM regions (all $p > 0.05$).

Exploratory TIME pattern grouping based on spatial heterogeneity. Unsupervised clustering of CD8/CD20-enriched and CD163/FOXP3-enriched proportions initially identified three exploratory TIME pattern groups (Figure 3A, Supplementary Figure S13A). However, stability analysis revealed mean Jaccard similarities of 0.93, 0.65, and 0.38 for the three clusters, respectively (Supplementary Figure S13B). The relatively low stability of Cluster 1 (Jaccard=0.38), combined with its inconsistency with established clinical frameworks, indicated that purely data-driven clustering was insufficient to define robust clinical categories. Therefore, to ensure clinical reproducibility and comparability with previously described frameworks [23-25], we applied predefined threshold-based rules (≥ 60%, < 40%, and 40-60%) to the original CD8/CD20 proportions to define the final exploratory TIME pattern groups (CD8/CD20-enriched, CD163/FOXP3-enriched, and intermediate). The distribution of CD8/CD20 proportions across the three clusters and the chosen thresholds are shown in Supplementary Figure S13C.

The distribution of these groups progressively shifted from the CD163/FOXP3-enriched pattern to the CD8/CD20-enriched pattern with increasing distance from the TC (Figure 3B), consistent with

the compositional gradient described above. Assessment of intratumoral heterogeneity revealed that 31% of patients exhibited low-grade heterogeneity, while 69% showed moderate or high heterogeneity (Figure 3C). Among the 32 low-heterogeneity patients, the CD163/FOXP3-enriched pattern predominated, accounting for 56.3% (18 cases), while the CD8/CD20-enriched and intermediate patterns each accounted for 21.9% (7 cases) (Figure 3D). Thus, spatial homogeneity was predominantly associated with the CD163/FOXP3-enriched pattern.

Exploratory TIME pattern groups in relation to clinicopathological features. TIME heterogeneity grade and the distribution of exploratory TIME pattern groups in the TC and IIM showed no significant association with clinicopathological factors (Supplementary Tables S12-S14). In the OIM, the distribution was associated with lymph node metastasis ($p < 0.001$), T stage ($p < 0.001$), and TNM stage ($p < 0.001$, Table 1).

For the survival analysis, baseline clinicopathological features were comparable between the 50 patients with complete data and the 52 patients lost to follow-up (all $p > 0.05$, Supplementary Table S15). The median follow-up was 38.5 months (95%CI: 35-43 months), with 11 recorded deaths. Numbers at risk are shown in Figure 4. No significant survival differences were observed among heterogeneity grades or exploratory TIME pattern groups (Figures 4A-4D).

In univariate Cox regression analyses (Supplementary Table S16), no variables including the exploratory TIME pattern groups, TIME heterogeneity grade, TNM stage, or other clinicopathological features were significantly associated with overall survival (all $p > 0.05$). Similarly, in four separate multivariate models adjusted for TNM stage (Supplementary Table S17), neither the TIME pattern groups (Models 1-3) nor the TIME heterogeneity grade (Model4) showed independent prognostic value (all $p > 0.05$). Due to the limited number of events (n=11), the confidence intervals were wide, indicating limited statistical precision.

Spatial distribution of PD-1$^+$ cells and SMA$^+$ stromal cells across tumor regions. To examine the spatial relationship between PD-1$^+$ cells and CD8$^+$ T cell distribution, we assessed PD-1 and CD8 by single-marker immunohistochemistry, together with SMA$^+$ stromal cells. The PD-1$^+$ cell density was highest in the OIM, significantly higher than in both the TC ($p < 0.01$) and IIM ($p < 0.001$) regions, whereas no significant difference was observed between the TC and IIM (Figures 5A, 5B; Supplementary Table S18). Regarding the PD-1$^+$/CD8$^+$ T cell ratio, both the TC and OIM regions exhibited significantly higher ratios than the IIM region ($p < 0.01$, Figure 5C;

Accepted manuscript

Supplementary Table S18). However, no significant difference was observed between the TC and OIM regions. Across exploratory TIME pattern groups in the OIM region, the CD8/CD20-enriched pattern exhibited the highest PD-1^+ cell density ($p < 0.05$), whereas the CD163/FOXP3-enriched pattern showed the lowest ($P < 0.05$ vs. CD8/CD20-enriched). However, no significant differences were observed among the three patterns in the TC and IIM regions (all $p > 0.05$; Figure 5D; Supplementary Table S19).

Concurrently, the density of SMA^+ stromal cells shifted toward lower values from the TC to the OIM, alongside a shift toward higher values for total immune infiltration (Supplementary Figures S14A, S14B). In terms of absolute quantities, SMA score showed a consistent and significant negative correlation with $CD8^+$ T cells across all three regions ($q < 0.001$). For $CD20^+$ B cells, significant negative correlations were observed in the TC and OIM ($q < 0.001$), and a weaker but significant negative correlation in the IIM ($q < 0.05$). In contrast, no significant correlations were found between SMA score and $CD163^+$ cells in any region. For $FOXP3^+$ T cells, a significant negative correlation was observed only in the OIM ($q < 0.01$), while no significant correlations were found in the TC and IIM (Supplementary Figure S14C; Supplementary Table S20). Additionally, SMA scores varied among TIME patterns in a region-dependent manner (Supplementary Figure S14D; Supplementary Table S21). The CD163/FOXP3-enriched pattern consistently exhibited the highest SMA scores, significantly exceeding the intermediate pattern in both the TC ($p < 0.05$) and IIM ($p < 0.01$) regions. In the OIM region, it further surpassed both the CD8/CD20-enriched and intermediate patterns ($p < 0.05$ for both). All other post-hoc comparisons were not significant. Collectively, these observations indicate significant spatial heterogeneity across tumor regions, characterized by a progressive decrease in SMA+ stromal cell scores from the TC to the OIM, an increase in CD8+ T cell infiltration in the OIM, and a U-shaped trend in the PD-1/CD8 ratio (higher in both the TC and OIM, but lower in the IIM).

Discussion

The enrichment of specific immune cells at the invasive margins observed in our study is consistent with a common spatial pattern in solid tumors: the tumor periphery represents a region of active immune–stromal interaction**.** This phenomenon, reported across cancer types [10, 12, 14, 27], has been associated with chemokine gradients and nutrient competition at the tumor-stroma interface

Accepted manuscript

[27]. Beyond cell density, the compositional shift from $CD163^+$ macrophage-like cells to $CD20^+$ B cells with increasing distance from the tumor center suggests a spatial transition in immune composition. This spatial pattern may reflect regional differences in the tumor microenvironment, in which the tumor core and outer margin display distinct immune–stromal features [14, 28-30].

This structural gradient was accompanied by region-dependent compositional differences. The variable correlations between $CD163^+$ macrophage-like cells and other immune cells suggest that the spatial relationship of a given cell type with other immune cells is context-dependent. For example, $CD163^+$ macrophage-like cells were positively associated with B cells in the central regions but negatively associated with $FOXP3^+$ T cells at the invasive margin, which may reflect distinct local microenvironments. The lack of association between $CD8^+$ T cell densities and aggressive clinical features, such as invasive depth, suggests that infiltration alone may not be sufficient for tumor control [31]. In contrast, the depth-dependent changes in $CD163^+$ macrophage-like cells and CD20+ B cells indicate that these subsets exhibit distinct spatial distribution patterns across different invasion depths. This spatial dissociation, which may involve local immune-regulatory networks [32-34], highlights the need to evaluate spatial immune composition, not just presence, when interpreting TIME data. Furthermore, neither Ki-67 status nor tumor differentiation was significantly associated with the density of any of the four immune cell types, suggesting that tumor cell-intrinsic features may not be the primary drivers of the spatial immune heterogeneity.

Our exploratory TIME pattern groups are broadly consistent with previously described frameworks [23-25], as they integrate compositional dimensions rather than relying solely on $CD8^+$ T-cell topography. The progressive shift from CD163/FOXP3-enriched to CD8/CD20-enriched patterns toward the tumor periphery may reflect regional differences in the tumor microenvironment. Notably, spatial homogeneity was predominantly associated with the CD163/FOXP3-enriched pattern, suggesting that a homogeneous TIME may often display this pattern.

This immune classification demonstrated region-specific clinicopathological associations. The association of OIM subtypes with lymph node metastasis, depth of invasion, and TNM stage suggests that the outer invasive margin is involved in tumor progression. These findings are consistent with the concept that lymphovascular and neural infiltration occur at the invasive front. However, when we extended these clinicopathological associations to survival outcomes, the Cox

regression analyses did not demonstrate independent prognostic value. This discrepancy may be attributed to the limited statistical power of this cohort and the confounding effects of adjuvant therapies. Because only 11 deaths occurred during follow-up, the negative survival findings should be interpreted as statistically inconclusive rather than evidence against a biological role for TIME features. Furthermore, the absence of a significant association between TIME heterogeneity grade and prognosis may reflect the complex and dynamic nature of the immune microenvironment. Future prospective studies with larger cohorts, extended follow-up, and spatial omics are warranted to validate these exploratory findings and clarify their clinical utility.

To explore potential factors associated with the spatial heterogeneity and region-specific features of the exploratory TIME pattern groups, we examined PD-1 expression and SMA^+ stromal cell distribution. Since PD-1 is predominantly expressed on $CD8^+$ T cells [35], the elevated PD-1/CD8 ratio in both the tumor center and the outer invasive margin, despite lower total $PD\text{-}1^+$ cells, suggests region-specific immune regulation. Previous studies have shown that PD-1 engagement is associated with $CD8^+$ T cell exhaustion and may contribute to the recruitment of immunosuppressive cells, facilitating tumor progression [36, 37]. Such region-specific immune regulation has been proposed to be associated with chronic antigen stimulation by poorly differentiated tumor cells [38], combined with metabolic stress and hypoxia. In the OIM region, the CD8/CD20-enriched pattern showed the highest PD-1 expression. Previous studies have suggested that PD-1 upregulation in the context of active T cell infiltration may reflect adaptive immune resistance [39], and whether such a state may benefit from immune checkpoint blockade requires further investigation in immunotherapy-treated cohorts [40]. Concurrently, because SMA staining was restricted to the tumor stromal compartment, excluding mucosal muscularis, muscularis propria, and perivascular regions, these SMA^+ stromal cells may predominantly represent myofibroblasts and a subset of cancer-associated fibroblasts (CAFs). Their inverse spatial relationship with immune cells, and the observation that SMA scores were highest in the CD163/FOXP3-enriched pattern [41, 42], suggest that these SMA^+ stromal cells are associated with the spatial distribution of immune cells. Together, these observations suggest that PD-1-related regulation and stromal components are associated with region-specific features of the spatial immune landscape, in which the tumor center and invasive margins may represent immunologically distinct compartments.

In summary, this study characterized the spatial heterogeneity of the gastric cancer TIME at the

Accepted manuscript

structural, functional, and clinical levels, and defined exploratory TIME pattern groups that reveal regional immune specialization and their association with clinicopathological features. However, the study is limited by the small number of patients with complete survival data (n=50), which likely underpowered the survival comparisons. In addition, PD-1 and CD8 were assessed separately, and the PD-1/CD8 ratio reflects relative single-marker densities rather than a functionally defined exhaustion state. Future investigations with larger cohorts and extended follow-up are warranted to validate these exploratory spatial patterns and to assess their clinical utility in immunotherapy-treated patients.

Acknowledgements: This work was supported by the National Natural Science Foundation of China with Grant Nos. 81871919 (LM), the Natural Science Foundation of Gansu Province with Grant Nos. 25JRRA652 (ZCL), The Fundamental Research Funds for the Central Universities with Grant Nos. 31920230194(SLN).

Supplementary data are available in the online version of the paper.

References

[1] JIA Q, WANG A, YUAN Y, ZHU B, LONG H. Heterogeneity of the tumor immune microenvironment and its clinical relevance. Exp Hematol Oncol 2022; 11: 24. https://doi.org/10.1186/s40164-022-00277-y

[2] CHEN YP, LV JW, MAO YP, LI XM, LI JY et al. Unraveling tumour microenvironment heterogeneity in nasopharyngeal carcinoma identifies biologically distinct immune subtypes predicting prognosis and immunotherapy responses. Mol Cancer 2021; 20: 14. https://doi.org/10.1186/s12943-020-01292-5

[3] WANG W, YE LF, BAO H, HU MT, HAN M et al. Heterogeneity and evolution of tumour immune microenvironment in metastatic gastroesophageal adenocarcinoma. Gastric Cancer 2022; 25: 1017-1030. https://doi.org/10.1007/s10120-022-01324-7

[4] KALBASI A, RIBAS A. Tumour-intrinsic resistance to immune checkpoint blockade. Nat Rev Immunol 2020; 20: 25-39. https://doi.org/10.1038/s41577-019-0218-4

[5] HAVEL JJ, CHOWELL D, CHAN TA. The evolving landscape of biomarkers for checkpoint inhibitor immunotherapy. Nat Rev Cancer 2019; 19: 133-150. https://doi.org/10.1038/s41568-019-0116-x

[6] HARTGRINK HH, JANSEN EP, VAN GRIEKEN NC, VAN DE VELDE CJ. Gastric cancer. Lancet 2009; 374: 477-490. https://doi.org/10.1016/S0140-6736(09)60617-6

[7] AOYAGI K. Molecular targeting to treat gastric cancer. World J Gastroenterol 2014; 20: 13741. https://doi.org/10.3748/wjg.v20.i38.13741

Accepted manuscript

[8] GULLO I, CARNEIRO F, OLIVEIRA C, ALMEIDA GM. Heterogeneity in gastric cancer: from pure morphology to molecular classifications. Pathobiology 2018; 85: 50-63. https://doi.org/10.1159/000473881

[9] FANG F, ZHANG T, LI Q, CHEN X, JIANG F et al. The tumor immune-microenvironment in gastric cancer. Tumori 2022; 108: 541-551. https://doi.org/10.1177/03008916211070051

[10] GUO S, CHEN X, GUO C, WANG W. Tumour-associated macrophages heterogeneity drives resistance to clinical therapy. Expert Rev Mol Med 2022; 24: e17. https://doi.org/10.1017/erm.2022.8

[11] WANG Z, DONG Z, ZHAO G, NI B, ZHANG ZZ. Prognostic role of myeloid-derived tumor-associated macrophages at the tumor invasive margin in gastric cancer with liver metastasis (GCLM): a single-center retrospective study. J Gastrointest Oncol 2022; 13: 1340-1350. https://doi.org/10.21037/jgo-22-530

[12] DONG L, PENG L, MA L, LIU D, ZHANG S et al. Heterogeneous immunogenomic features and distinct escape mechanisms in multifocal hepatocellular carcinoma. J Hepatol 2020; 72: 896-908. https://doi.org/10.1016/j.jhep.2019.12.014

[13] LIN S, SUN Y, CAO C, ZHU Z, XU Y et al. Single-nucleus RNA sequencing reveals heterogenous microenvironments and specific drug response between cervical squamous cell carcinoma and adenocarcinoma. eBioMedicine 2023; 97: 104846. https://doi.org/10.1016/j.ebiom.2023.104846

[14] VALENZUELA-MEMBRIVES MDM, PEREA-GARCÍA F, SANCHEZ-PALENCIA A, RUIZ-CABELLO F, GÓMEZ-MORALES M et al. Progressive changes in composition of lymphocytes in lung tissues from patients with non-small-cell lung cancer. Oncotarget 2016; 7: 71608-71619. https://doi.org/10.18632/oncotarget.12264

[15] ZHAO Y, FU X, LOPEZ JI, ROWAN A, AU L et al. Selection of metastasis competent subclones in the tumour interior. Nat Ecol Evol 2021; 5: 1033-1045. https://doi.org/10.1038/s41559-021-01456-6

[16] WU L, YAN J, BAI Y, CHEN F, ZOU X et al. An invasive zone in human liver cancer identified by Stereo-seq promotes hepatocyte-tumor cell crosstalk, local immunosuppression and tumor progression. Cell Res 2023; 33: 585-603. https://doi.org/10.1038/s41422-023-00831-1

[17] MASUGI Y, ABE T, UENO A, FUJII-NISHIMURA Y, OJIMA H et al. Characterization of spatial distribution of tumor-infiltrating CD8+ T cells refines their prognostic utility for pancreatic cancer survival. Mod Pathol 2019; 32: 1495-1507. https://doi.org/10.1038/s41379-019-0291-z

[18] SOERATRAM TTD, BIESMA HD, EGTHUIJSEN JMP, MEERSHOEK-KLEIN KRANENBARG E, HARTGRINK HH et al. Prognostic value of T-cell density in the tumor center and outer margins in gastric cancer. Mod Pathol 2023; 36: 100218. https://doi.org/10.1016/j.modpat.2023.100218

[19] JUHÁSZ P, HASULYÓ D, BEDEKOVICS J, BEKE L, KACSALA N et al. Carbonic anhydrase IX (CAIX) expressing hypoxic micro-environment hampers CD8+ immune cell infiltrate in breast carcinoma. Appl Immunohistochem Mol Morphol 2023; 31: 26-32. https://doi.org/10.1097/PAI.0000000000001082

[20] ASHIMOV EA, CHICHEVATOV DA, RADOVSKY VV, KOLESNIKOVA EA, KLIMIN SA et al. Determination of the ki-67 threshold value for predicting lymph nodes involvement

Accepted manuscript

in patients with gastric cancer. Malig Tumours 2024; 14: 21-29. https://doi.org/10.18027/2224-5057-2024-14-1-21-29

[21] ACS B, PELEKANOU V, BAI Y, MARTINEZ-MORILLA S, TOKI M et al. Ki67 reproducibility using digital image analysis: an inter-platform and inter-operator study. Lab Invest 2019; 99: 107-117. https://doi.org/10.1038/s41374-018-0123-7

[22] ALAM MR, SEO KJ, YIM K, LIANG P, YEH J et al. Comparative analysis of Ki-67 labeling index morphometry using deep learning, conventional image analysis, and manual counting. Transl Oncol 2025; 51: 102159. https://doi.org/10.1016/j.tranon.2024.102159

[23] DEBROY S, BHAKE AS. Tumour-infiltrating lymphocytes and its association with prognostic pathological parameters in resectable oral squamous cell carcinoma: an observational ambispective study research protocol. J Clin Diagn Res 2026; 20: EK05-EK08. https://doi.org/10.7860/JCDR/2026/87433.24146

[24] INTARAWICHIAN P, SANGPAIBOOL S, PRAJUMWONGS P, SA-NGIAMWIBOOL P, SANGKHAMANON S et al. Prognostic significance of tumor-infiltrating lymphocytes in predicting outcome of distal cholangiocarcinoma in Thailand. Front Oncol 2022; 12: 1004220. https://doi.org/10.3389/fonc.2022.1004220

[25] DULGAR O, ILVAN S, TURNA ZH. Prognostic factors and tumor infiltrating lymphocytes in triple negative breast cancer. Eur J Breast Health 2020; 16: 276-281. https://doi.org/10.5152/ejbh.2020.5305

[26] MAQSOOD A, ALI A, ZAFFAR Z, MOKEEM S, MOKEEM SS et al. Expression of CD34 and α-SMA markers in oral squamous cell carcinoma differentiation: a histological and histo-chemical study. Int J Environ Res Public Health 2020; 18: 192. https://doi.org/10.3390/ijerph18010192

[27] FU T, DAI LJ, WU SY, XIAO Y, MA D et al. Spatial architecture of the immune microenvironment orchestrates tumor immunity and therapeutic response. J. Hematol Oncol 2021; 14: 98. https://doi.org/10.1186/s13045-021-01103-4

[28] ZHANG AW, MCPHERSON A, MILNE K, KROEGER DR, HAMILTON PT et al. Interfaces of malignant and immunologic clonal dynamics in ovarian cancer. Cell 2018; 173: 1755-1769. https://doi.org/10.1016/j.cell.2018.03.073

[29] HUANG YK, WANG M, SUN Y, DI COSTANZO N, MITCHELL C et al. Macrophage spatial heterogeneity in gastric cancer defined by multiplex immunohistochemistry. Nat Commun 2019; 10: 3928. https://doi.org/10.1038/s41467-019-11788-4

[30] AOKI T, CHONG LC, TAKATA K, MILNE K, HAV M et al. Single-cell transcriptome analysis reveals disease-defining T-cell subsets in the tumor microenvironment of classic Hodgkin lymphoma. Cancer Discov 2020; 10: 406-421. https://doi.org/10.1158/2159-8290.CD-19-0680

[31] LV B, WANG Y, MA D, CHENG W, LIU J et al. Immunotherapy: reshape the tumor immune microenvironment. Front Immunol 2022; 13: 844142. https://doi.org/10.3389/fimmu.2022.844142

[32] DOLINA JS, VAN BRAECKEL-BUDIMIR N, THOMAS GD, SALEK-ARDAKANI S. CD8+ T cell exhaustion in cancer. Front Immunol 2021; 12: 715234. https://doi.org/10.3389/fimmu.2021.715234

[33] MCLANE LM, ABDEL-HAKEEM MS, WHERRY EJ. CD8 T cell exhaustion during chronic viral infection and cancer. Annu Rev Immunol 2019; 37: 457-495. https://doi.org/10.1146/annurev-immunol-041015-055318

Accepted manuscript

[34] BELK JA, DANIEL B, SATPATHY AT. Epigenetic regulation of T cell exhaustion. Nat Immunol 2022; 23: 848-860. https://doi.org/10.1038/s41590-022-01224-z
[35] CHEN K, WANG X, YANG L, CHEN Z. The anti-PD-1/PD-L1 immunotherapy for gastric esophageal cancer: a systematic review and meta-analysis and literature review. Cancer Control 2021; 28: 1073274821997430. https://doi.org/10.1177/1073274821997430
[36] HAN Y, LIU D, LI L. PD-1/PD-L1 pathway: current researches in cancer. Am J Cancer Res 2020; 10: 727-742.
[37] WANG Q, BARDHAN K, BOUSSIOTIS VA, PATSOUKIS N. The PD-1 interactome. Adv Biol 2021; 5: 2100758. https://doi.org/10.1002/adbi.202100758
[38] HSIEH WC, BUDIARTO BR, WANG YF, LIN CY, GWO MC et al. Spatial multi-omics analyses of the tumor immune microenvironment. J Biomed Sci 2022; 29: 96. https://doi.org/10.1186/s12929-022-00879-y
[39] CHOO J, KUA LF, SOE MY, ASUNCION BR, TAN BKJ et al. Clinical relevance of PD-1 positive CD8 T-cells in gastric cancer. Gastric Cancer 2023; 26: 393-404. https://doi.org/10.1007/s10120-023-01364-7
[40] BAGAEV A, KOTLOV N, NOMIE K, SVEKOLKIN V, GAFUROV A et al. Conserved pan-cancer microenvironment subtypes predict response to immunotherapy. Cancer Cell 2021; 39: 845-865. https://doi.org/10.1016/j.ccell.2021.04.014
[41] FREEMAN P, MIELGO A. Cancer-associated fibroblast mediated inhibition of CD8+ cytotoxic T cell accumulation in tumours: mechanisms and therapeutic opportunities. Cancers 2020; 12: 2687. https://doi.org/10.3390/cancers12092687
[42] MAO X, XU J, WANG W, LIANG C, HUA J et al. Crosstalk between cancer-associated fibroblasts and immune cells in the tumor microenvironment: new findings and future perspectives. Mol Cancer 2021; 20: 131. https://doi.org/10.1186/s12943-021-01428-1

Figure Legends

Figure 1. Spatial heterogeneity characteristics of the TIME structure. Representative images of immune cell infiltration in tumor-related regions (scale bars: 50 μm): A) TC; B) IIM; C) OIM. D) Immune infiltration status of gastric cancer patients in the TCGA database. E. Proportions of immune cell infiltration in different regions. (A-C) Friedman test followed by Dunnett's multiple comparison test; *$p < 0.05$, **$p < 0.01$, ***$p < 0.001$. E) Wilcoxon paired signed-rank test with Benjamini-Hochberg FDR correction, Q=1%; ns, $q \geq 0.01$; **$q < 0.01$; ***$q < 0.001$. Detailed statistical parameters are provided in the corresponding Supplementary Tables S5 and S7.) Abbreviations: TC-tumor center; IIM-inner invasive margin; OIM-outer invasive margin; n=102 patients

Figure 2. Association between tumor proliferation and immune cell infiltration density in the TC region. A) Representative immunohistochemical images of Ki-67, CD8, CD20, CD163, and FOXP3.

Accepted manuscript

B) Comparisons of immune cell densities between Ki-67 High and Low groups (Wilcoxon matched-pairs signed rank test, n=57pairs; ns, $p > 0.05$; *$p < 0.05$; **$p < 0.01$; ***$p < 0.001$. Detailed statistical parameters are provided in Supplementary Table S9).

Figure 3. Spatial distribution and heterogeneity characteristics of exploratory TIME pattern groups. A) Schematic diagrams of the three exploratory TIME pattern groups; B) Proportions of exploratory TIME patterns in three tumor-related regions (n=102); C) Proportions of TIME heterogeneity grades (n=102); D) Distribution of exploratory TIME patterns in patients with heterogeneity grade I (n=32).

Figure 4. Kaplan-Meier curves for overall survival stratified by TIME heterogeneity grade and exploratory TIME pattern groups. A) TIME heterogeneity grade. B) TIME pattern groups in the tumor center (TC). C) TIME pattern groups in the inner invasive margin (IIM). D) TIME pattern groups in the outer invasive margin (OIM). 1, CD8/CD20-enriched group; 2, CD163/FOXP3-enriched group; 3, intermediate group. Numbers at risk are shown below each panel; p-values were calculated using the log-rank test

Figure 5. Predictive role of exploratory TIME patterns in the response of gastric carcinoma patients to anti-PD-1 therapy. A) Representative images of PD-1+ cells in different tumor-related regions; B) Statistical chart of PD-1+ cell density in different tumor-related regions; C) Ratios of PD-1+ cells to CD8+ T cells in the three regions; D) Statistical graphs of PD-1+ cell density among different exploratory TIME patterns in the TC, IIM, and OIM regions. (B, C) Wilcoxon matched-pairs signed-rank test with Benjamini-Hochberg FDR correction, Q=1%, $q < 0.01$ was considered significant, n=95 pairs; D) Kruskal-Walli's test followed by Dunn`s multiple comparison test, n=95. B, C) ns, $q \geq 0.01$; **$q < 0.01$; ***$q < 0.001$. D) ns, $p > 0.05$; *$p < 0.05$. Detailed statistical parameters are provided in Supplementary Tables S18 and S19.)

Accepted manuscript

605 **Table 1.** Association between exploratory TIME pattern groups in the outer invasive margin (OIM) and clinicopathological factors in gastric cancer
606 patients (n=102).

Variables	CD8/CD20-enriched		CD163/FOXP3-enriched		Intermediate		p-value	*V*
	n (%)	95%CI	n (%)	95%CI	n (%)	95%CI		
Gender							0.39	0.14
Male	24 (33.8)	23.0-45.0	16 (22.5)	14.0-34.0	31 (43.7)	32.0-55.0		
Female	9 (29.0)	16.0-47.0	11 (35.5)	21.0-53.0	11 (35.5)	21.0-53.0		
Age (years)							0.71	0.08
<60	18 (35.3)	24.0-49.0	14 (27.5)	17.0-41.0	19 (37.3)	25.0-51.0		
≥60	15 (29.4)	19.0-43.0	13 (25.5)	16.0-39.0	23 (45.1)	32.0-59.0		
LNM							< 0.001	0.44
No	27 (50.9)	38.0-64.0	13 (24.5)	15.0-38.0	13 (24.5)	15.0-38.0		
Yes	6 (12.2)	6.0-24.0	14 (28.6)	18.0-42.0	29 (59.2)	45.0-72.0		
T stage							< 0.001	0.46
T1+T2	18 (69.2)	50.0-83.0	4 (15.4)	6.0-34.0	4 (15.4)	6.0-34.0		
T3+T4	15 (19.7)	12.0-30.0	23 (30.3)	21.0-41.0	38 (50.0)	39.0-61.0		
PNI							0.06	0.23
No	23 (42.6)	30.0-56.0	12 (22.2)	13.0-35.0	19 (35.2)	24.0-49.0		
Yes (	10 (20.8)	12.0-34.0	15 (31.3)	20.0-45.0	23 (47.9)	34.0-62.0		
LVIE							0.25	0.16
No	29 (34.9)	26.0-46.0	23 (27.7)	19.0-38.0	31 (37.3)	28.0-48.0		
Yes	4 (21.1)	9.0-43.0	4 (21.1)	9.0-43.0	11 (57.9)	36.0-77.0		
TNM stage							< 0.001	0.31
I	21 (56.8)	41.0-71.0	5 (13.5)	6.0-28.0	11 (29.7)	17.0-46.0		
I	8 (29.6)	16.0-48.0	9 (33.3)	19.0-52.0	10 (37.0)	22.0-56.0		
I	4 (10.5)	4.0-24.0	13 (34.2)	21.0-50.0	21 (55.3)	40.0-70.0		
Lauren classification							0.97	0.05

Accepted manuscript

Intestinal	9 (31.0)	17.0-49.0	9 (31.0)	17.0-49.0	11 (38.0)	23.0-56.0
Diffuse	10 (33.3)	19.0-51.0	7 (23.3)	12.0-41.0	13 (43.3)	27.0-61.0
Mixed	14 (32.6)	20.0-47.0	11 (25.6)	15.0-40.0	18 (41.9)	28.0-57.0

607 Note: Data are presented as n (%) and 95%CI; p-values were calculated using Chi-square or Fisher's exact tests; V, Cramer's V; $p < 0.05$ was
608 considered significant
609 Abbreviations: TIME-tumor immune microenvironment; LNM-Lymph node metastasis; PNI-perineural invasion; LVIE-Lymphovascular tumor
610 emboli

Accepted manuscript

Fig. 1 [Download full resolution image]

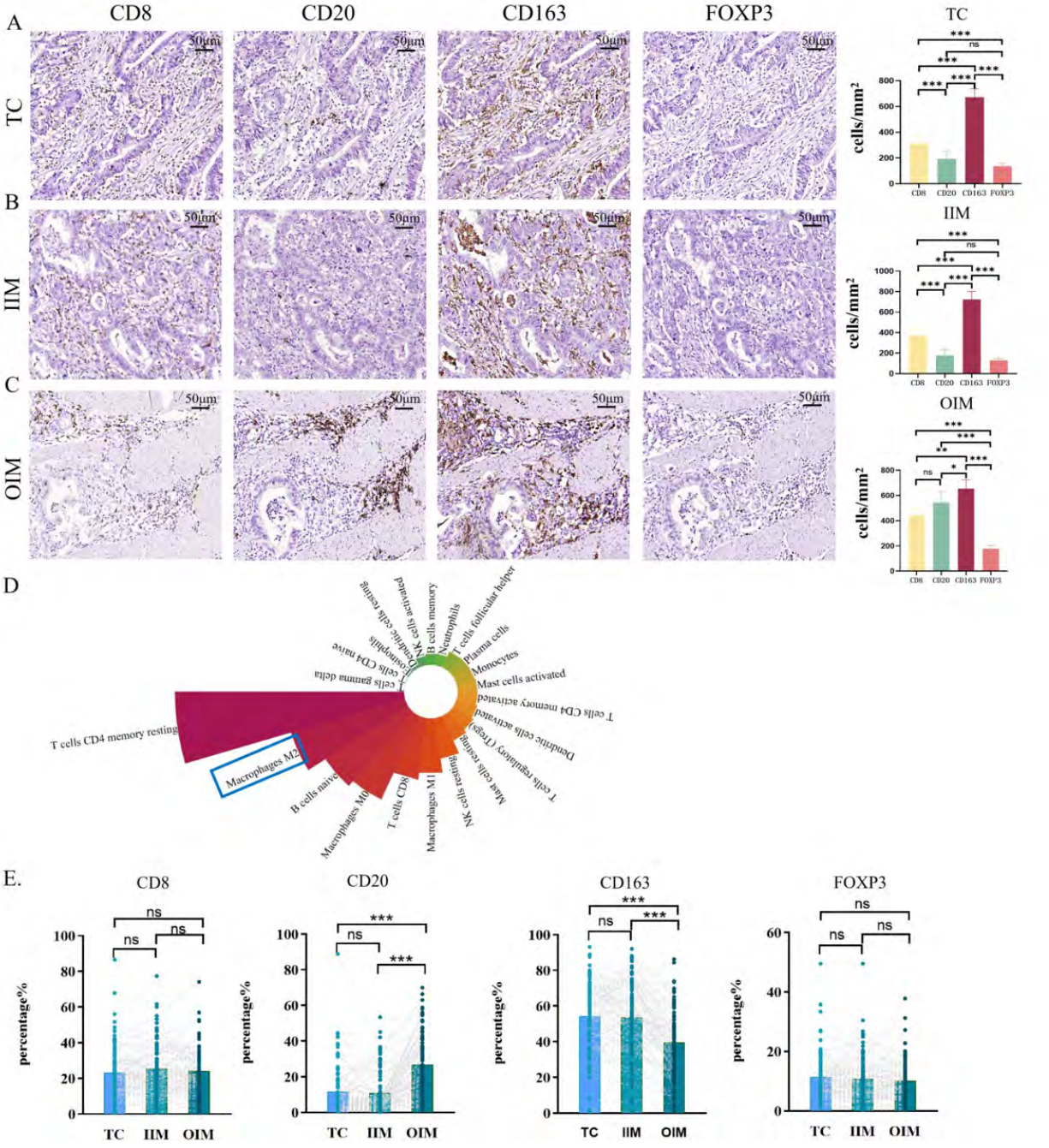

Fig. 2 Download full resolution image

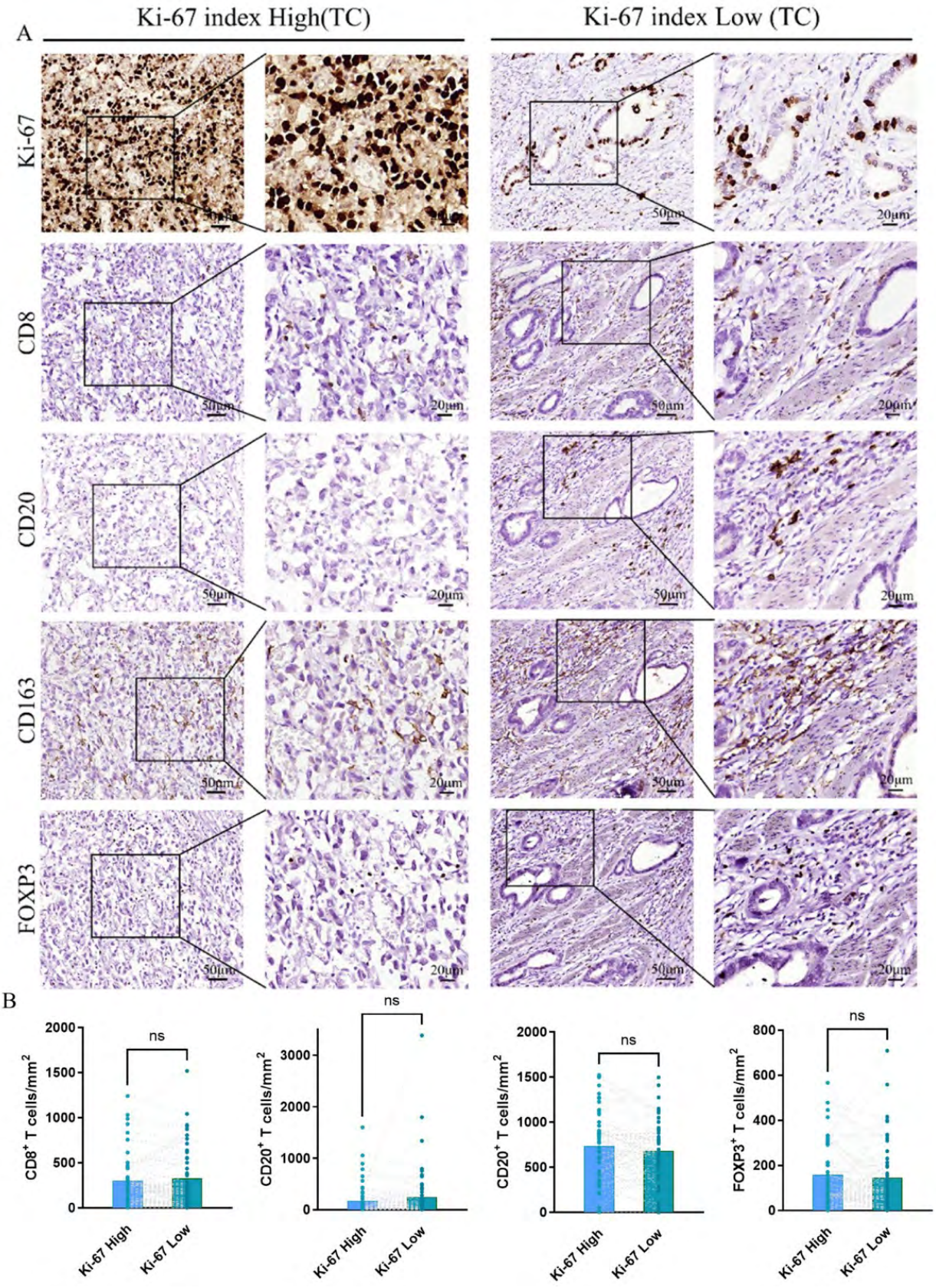

Fig. 3 Download full resolution image

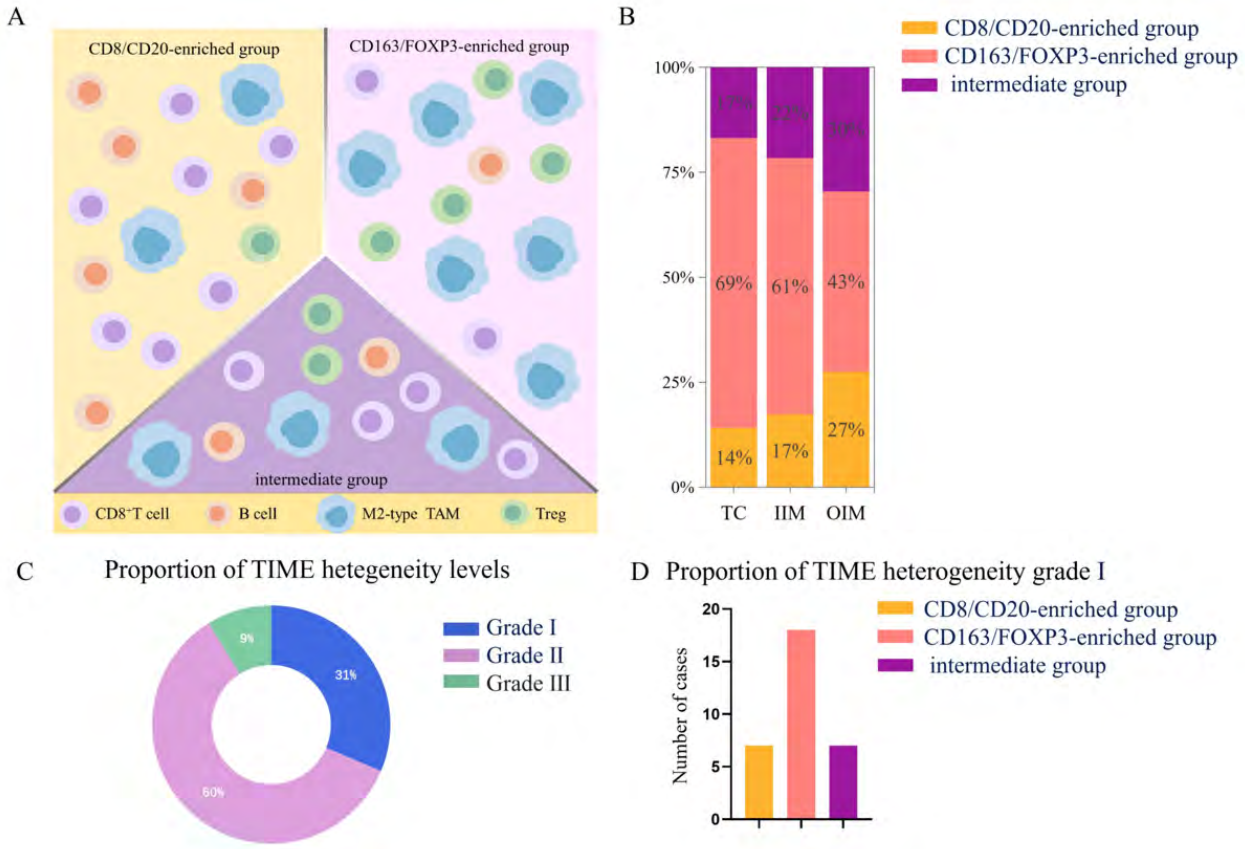

Fig. 4 Download full resolution image

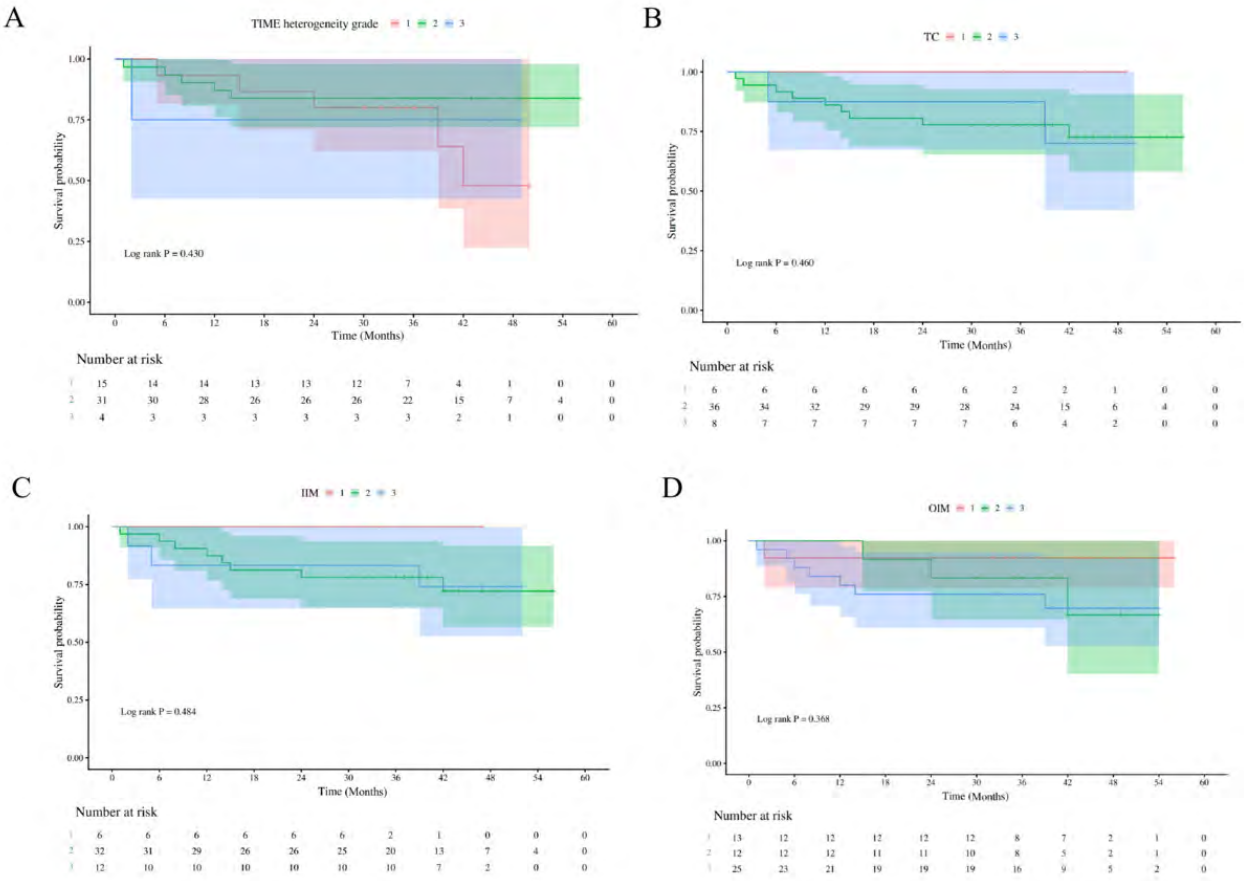

Fig. 5 Download full resolution image

